Characterization of an Orthotopic Rat Model of Glioblastoma Using Multiparametric Magnetic Resonance Imaging and Bioluminescence Imaging

Trung N.T. Le[1,2], Heeseung Lim[1,2], Amanda M. Hamilton[2], Katie M. Parkins[1,2], Yuanxin Chen[2], Timothy J. Scholl[1,2,3], and John A. Ronald[1,2,4]

[1]Department of Medical Biophysics, Western University, London, ON, Canada; [2]Robarts Research Institute, Western University, London, ON, Canada; [3]Ontario Institute for Cancer Research, Toronto, ON, Canada; and [4]Lawson Health Research Institute, London, ON, Canada

Corresponding Author:
John A. Ronald, PhD
Robarts Research Institute, Western University, 1151 Richmond Street North, Rm. 2241A, London, ON, Canada N6A 5B7;
E-mail: jronald@robarts.ca

Key Words: glioblastoma multiforme, C6 glioma rat, orthotopic, magnetic resonance imaging, bioluminescence imaging

Abbreviations: Glioblastoma multiforme (GBM), multiparametric magnetic resonance imaging (mpMRI), bioluminescence imaging (BLI), magnetic resonance imaging (MRI), apparent diffusion coefficients (ADC), fluorescence-activated cell sorting (FACS), gadolinium-diethylenetriaminepentacetate (Gd-DTPA), diffusion tensor imaging (DTI), contrast-enhanced (CE), repetition time (TR), echo time (TE), field of view (FOV), number of averages (NEX), region of interest (ROI), noncontrast-enhanced (NCE), magnetic resonance (MR), hematoxylin and eosin (H&E), magnetic resonance spectroscopic imaging (MRSI)

ABSTRACT

Glioblastoma multiforme (GBM) is the most common primary brain tumor, with most patients dying within 15–18 months of diagnosis despite aggressive therapy. Preclinical GBM models are valuable for exploring GBM progression and for evaluating new therapeutics or imaging approaches. The rat C6 glioma model shares similarities with human GBM, and application of noninvasive imaging enables better study of disease progression. Here, multiparametric magnetic resonance imaging (mpMRI) and bioluminescence imaging (BLI) were applied to characterize longitudinal development of orthotopic luciferase-expressing C6 tumors. Across all rats ($n = 11$), a large variability was seen for BLI signal, a relative measure of C6 cell viability, but in most individuals, BLI signal peaked at day 11 and decreased thereafter. T2 and contrast-enhanced T1 tumor volumes significantly increased over time ($P < .05$), and volume measures did not correlate with BLI signal. After day 11, tumor regions of noncontrast enhancement appeared in postcontrast T1-weighted magnetic resonance imaging, and had significantly higher apparent diffusion coefficient values compared with contrast-enhanced regions ($P < .05$). This suggests formation of ill-perfused, necrotic regions beyond day 11, which were apparent at end-point–matched tissue sections. Our study represents the first combined use of BLI and mpMRI to characterize the progression of disease in the orthotopic C6 rat model, and it highlights the variability in tumor growth, the complementary information from BLI and mpMRI, and the value of multimodality imaging to better characterize tumor development. Future application of these imaging tools will be useful for evaluation of treatment response, and should be pertinent for other preclinical models.

INTRODUCTION

Glioma is the most common malignant form of primary brain tumor with the highest mortality rate (1). Grade IV glioblastoma multiforme (GBM) is considered the most aggressive, invasive, and lethal form of glioma, and it accounts for ~50% of all glioma cases (2-4). GBM is considered almost invariably incurable, and patient survival after diagnosis is ~15–18 months despite aggressive treatment paradigms such as combined surgical resection (5), radiotherapy, and temozolomide (TMZ) chemotherapy (6, 7). These highly aggressive malignancies are exceedingly invasive and proliferative (8, 9), have robust angiogenesis, and are resistant to apoptosis (10, 11). Combined, these factors contribute to therapeutic resistance and nearly 100% recurrence rates. To better study the natural progression of this devastating disease and for enhanced evaluation of new treatment regimens, ways of noninvasively and longitudinally characterizing GBM tumors in both preclinical GBM models and GBM patients are highly sought.

Preclinical glioma models have been invaluable for understanding patient GBM progression, for evaluating promising therapeutic strategies, and for developing new noninvasive imaging techniques to aid better tumor characterization (12-14). In par-

ISSN 2379-1381 http://dx.doi.org/10.18383/j.tom.2018.00012

ticular, the orthotopic C6 rat model has provided considerable insight into the progression of GBM and the biological mechanisms regulating it (8, 13, 15-17). The C6 cell line was first developed by the Sweet Laboratory in the 1960s by means of repeated intravenous administration of the carcinogenic alkylating agent N-methyl-N-nitrosourea to outbred adult Wistar rats (18, 19). Since then, C6 cells have been isolated and grown in culture, and these can be used to generate orthotopic syngeneic tumors in rats. Orthotopic C6 tumors share several specific tumor markers found in human GBM such as increased *Ras* pathway activity, as well as increased expression of platelet-derived growth factor-beta, insulin-like growth factor 1, epidermal growth factor receptor, human epidermal growth factor receptor 3, and glial fibrillary acidic protein (13). C6 tumors also share histopathological features found in human GBM, particularly a diffuse infiltrative pattern (8). Because of these favorable characteristics, C6 tumor-bearing rats have been used to evaluate therapeutic efficacy of various treatment regimens such as chemotherapy (15), radiotherapy (16), and cytotoxic gene therapy (17), among others.

To facilitate improved evaluation of treatments and to better understand tumor progression in the C6 model, numerous groups have used clinically relevant imaging tools such as positron emission tomography (20), computed tomography (21), and magnetic resonance imaging (MRI) (22). MRI has become the standard of care for the detection, staging, and assessment of treatment response in patients with glioma (23). The benefits of MRI include the ability to collect high-resolution images (hundreds of microns) with excellent soft tissue contrast without the use of ionizing radiation, allowing for changes in tumor morphology to be sensitively monitored over time. Various MRI contrast mechanisms are available, which can accentuate different tumor features, allowing better delineation of tumor boundaries and intratumoral features such as edema, necrosis, or hemorrhage. Multiparametric MRI (mpMRI) describes the collection of a suite of MRI images with different contrast mechanisms, providing both anatomical and functional information about tumors that can include total tumor volume, contrast-enhanced tumor volume, apparent diffusion coefficients (ADC), and measures of perfusion (24). mpMRI has previously been applied to the orthotopic C6 rat model (22, 25-27). For instance, Liao et al. used mpMRI to gather information about tumor volume and location, blood–brain barrier integrity, and edema in the C6 model (28).

In addition to MRI, preclinical molecular imaging modalities can provide complementary information on tumor biology. Bioluminescence imaging (BLI) requires cells to be engineered to express a luciferase reporter gene before implantation into animals. Thereafter, following administration of the appropriate luciferin substrate, one can collect the light produced by these engineered cells by means of a cooled charged-coupled device camera (29). BLI provides the ability to sensitively monitor the relative viability of cancer cells over time because of the requirement of cells to actively transcribe the reporter, as well as adenosine triphosphate (ATP) as a cofactor for light production. The main purposes of this study were to use BLI to track the viability of C6 tumors growing orthotopically in Wistar rats, as well as the combined use of BLI and mpMRI to explore a relationship between tumor viability and tumor volume in this model. We found that the combined use of this suite of imaging tools provided new insights into individual rat tumor development in this model and will be useful for more precise evaluation of the effectiveness of new treatment strategies aimed at halting or preventing tumor progression.

METHODOLOGY

Cell Culture

C6 rat glioma cells (CCL-107, American Type Culture Collection, Manassas, VA) were grown in Ham's F-12K (Kaighn's) medium (ThermoFisher Scientific, Waltham, MA) containing 2.5% fetal bovine serum, 15% horse serum, and 1% penicillin–streptomycin. All cells were grown at 37°C in a 5% CO_2 incubator. Cells were regularly confirmed to be mycoplasma-negative using the MycoAlert Mycoplasma Detection Kit (Lonza, Basel, Switzerland).

Cell Modification

Self-inactivating lentiviral particles coexpressing the red-shifted *Luciola italica* luciferase (Luc) and green fluorescent protein (GFP) under the control of the Ubiquitin C promoter were used (RediFect Red-FLuc-GFP; PerkinElmer, Waltham, MA; Figure 1A). For efficient coexpression, Luc and GFP are separated by a T2A self-cleaving peptide in this vector. C6 glioma cells were transduced for 24 hours at a viral multiplicity of infection of 50 using polybrene (8 μg/mL). Following transduction, fluorescence-activated cell sorting (FACS) was performed twice on modified C6 cells to select for the highest GFP-expressing cells using a BD FACSAria™ III sorter (BD Biosciences, Franklin Lakes, NJ).

Cell Doubling Rate

Naïve C6, modified luciferase-expressing C6 cells (C6Luc) without D-Luciferin and C6Luc cells incubated with 150 μg/mL of D-luciferin (C6Luc150) were seeded into individual wells of a 6-well plate (2×10^3 cells/well; $n = 6$ per cell condition). Every 24 hours for up to 144 hours, the total cell number from 1 well per cell condition was quantified using a hemocytometer. The doubling rates of the cell conditions were determined using the model $y = a \times 2^{t/b}$; here, y is the cell count, a is the number of cells in the initial seed, t is the amount of time elapsed in hours, and b is the doubling time of the cells in hours. A MATLAB script using the nonlinear least squares trust-region algorithm from the Curve Fitting Toolbox (MATLAB 2016b, The MathWorks Inc., Natick, MA) was used to determine parameters a and b.

BLI Signal vs Cell Number

C6Luc cells (1×10^6, 5×10^5, 2.5×10^5, 1.25×10^5, 6.25×10^4, and 3.13×10^4) were seeded into individual wells and incubated for 24 hours ($n = 3$). D-luciferin (150 μg/mL) was added to each well, and plates were imaged 5 minutes later with an IVIS Lumina XRMS In Vivo Imaging System (PerkinElmer). Images were analyzed using Living Image Software (IVIS Imaging Systems, PerkinElmer) to obtain the average radiance (photons/sec/cm^2/steradian) per well.

Orthotopic C6 Glioma Rat Model

All animal procedures were performed in accordance with relevant guidelines and regulations stipulated by an animal use protocol approved by the University Council on Animal Care, Animal Use Subcommittee at Western University (Animal Use

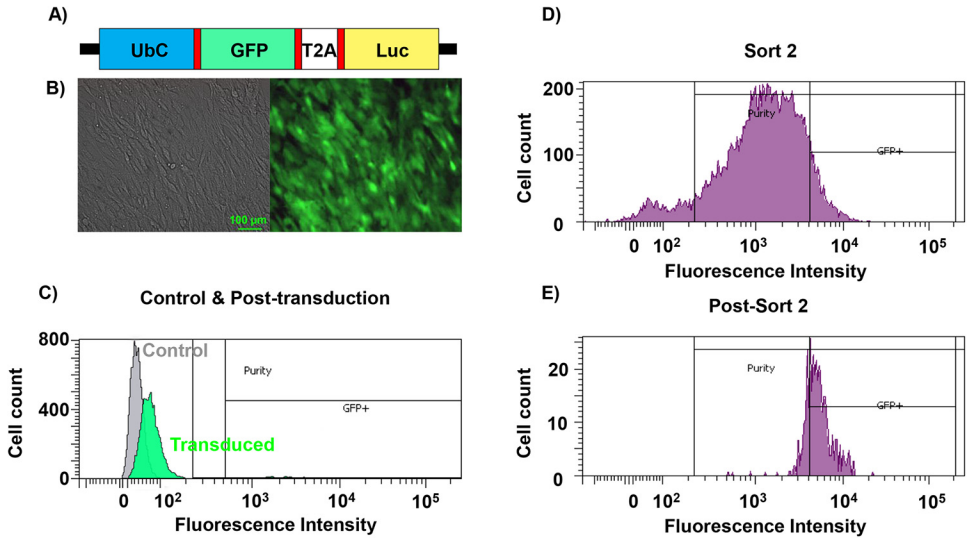

Figure 1. Lentiviral modification of C6 glioma cells with reporter genes. Expression cassette of *Luciola italica* luciferase (Luc)-green fluorescent protein (GFP) lentiviral vectors (A). Left: bright field image of C6Luc cells postsort in vitro; Right: fluorescence image of the GFP expression. Scale bar = 100 μm (B). Fluorescence-activated cell sorting (FACS) of control (naïve C6; gray) and C6Luc (green) cells post transduction (C). Cells were gated to obtain the brightest GFP-expressing cells; 4.52% of all glioma cells. Second FACS to select the top 10% of GFP-expressing cells after propagation of highest GFP-expressing cells from the initial FACS (D). Immediately after the second FACS (D), a FACS was performed to evaluate GFP expression in the final population (100% of cells expressed GFP) (E).

Protocol: 2010-040). Male Wistar rats (n = 12; age, 4–6 weeks; weight, 200–225 g; Charles River Laboratories, Wilmington, MA) were used. Rats were anesthetized with 5% isoflurane, maintained at 2% isoflurane (1 L/min oxygen), and placed in a stereotactic frame for C6Luc cell implantation (Stoelting Co., IL). Fur on the superior side of the head was removed to expose the skin, and the bregma was landmarked after incision. A burr hole was drilled 1-mm anterior and 3-mm lateral to the bregma on the right. A microsyringe (Hamilton 1700 series) containing 10^6 C6Luc cells suspended in 10 μL of Hank's buffered salt solution at 37°C was advanced to a depth of 4 mm in the brain. The cells were injected at a rate of 3 μL/min. Bone wax was used to fill the burr hole to prevent cell suspension reflux. The incision was sutured and 1 mL of Meloxicam (5 mg/mL; Metacam, Boehringer Ingelheim Vetmedica, Ingelheim, Germany) was administered via a subcutaneous injection.

Imaging

Each animal was imaged 4, 8, 11, 15, and 18 days post cell implantation. Before each imaging session, all animals were anesthetized with isofluorane and a tail-vein catheter inserted and secured to enable injection of the MRI contrast agent, gadolinium-diethylenetriaminepentacetate (Gd-DTPA). During longitudinal imaging, 1 rat was euthanized before the end point because of a rapidly increasing tumor burden and deteriorating health; data from this animal were omitted.

BLI. Anesthetized rats were given an intraperitoneal injection of D-Luciferin (150 mg/kg; PerkinElmer) and imaged using the same imaging system mentioned above. To avoid imaging through the burr hole, animals were placed on their left side (tumor side closest to the camera) and images were collected for up to 30 minutes post injection with the following parameters: exposure time = 1 minute, binning factor = 8, f-stop = 1, and field-of-view = 12.5 cm.

mpMRI. Animals were imaged on a 3-Tesla (T) MRI scanner (Discovery MR750 3.0 T, General Electric Healthcare, IL). The heads of the anesthetized rats were placed inside an 8-rung, 33-mm-inside-diameter bird cage radiofrequency coil (Morris Instruments Inc., Ontario, Canada), which was located within a custom-built insertable gradient coil (30). Each MRI session consisted of the following: T2-weighted imaging, diffusion tensor imaging (DTI); and pre- and postcontrast-enhanced (CE) T1-weighted imaging after intravenous tail-vein administration of Gd-DTPA (0.5 mmol/kg; Magnevist, Bayer, Leverkusen, Germany). 3D T2-weighted images were collected using a 3D fast spin-echo (CUBE, General Electric Healthcare) sequence with the following parameters: repetition time (TR) = 4000 milliseconds, echo time (TE) = 62 milliseconds, echo train length = 160, field of view (FOV) = 60 × 30 × 30 mm, acquisition matrix = 128 × 128 × 100, section thickness = 0.6 mm, bandwidth = 62.5 kHz, and number of averages (NEX) = 9. DTI images were obtained using a 2D spin-echo single-section echo-planar imaging sequence with the following parameters: TR = 6000 milliseconds, TE = 71.1 milliseconds, FOV = 60 × 60 mm, acquisition matrix = 120 × 120, coronal sections = 130, section thickness = 3 mm, bandwidth = 166.7 kHz, NEX = 1, b-value = 1000 s/mm^2. Pre-CE (n = 5) and post-CE T1-weighted images were obtained using a 3D ultrafast gradient-recalled echo sequence for brain volume imaging (Fast GRE BRAVO, General Electric Healthcare) with the following parameters: TR = 6.9 milliseconds, TE = 2.9 milliseconds, preparation time = 450 milliseconds, FOV = 60 × 30 × 30 mm, acquisition matrix = 120 × 120 × 60, section thickness =

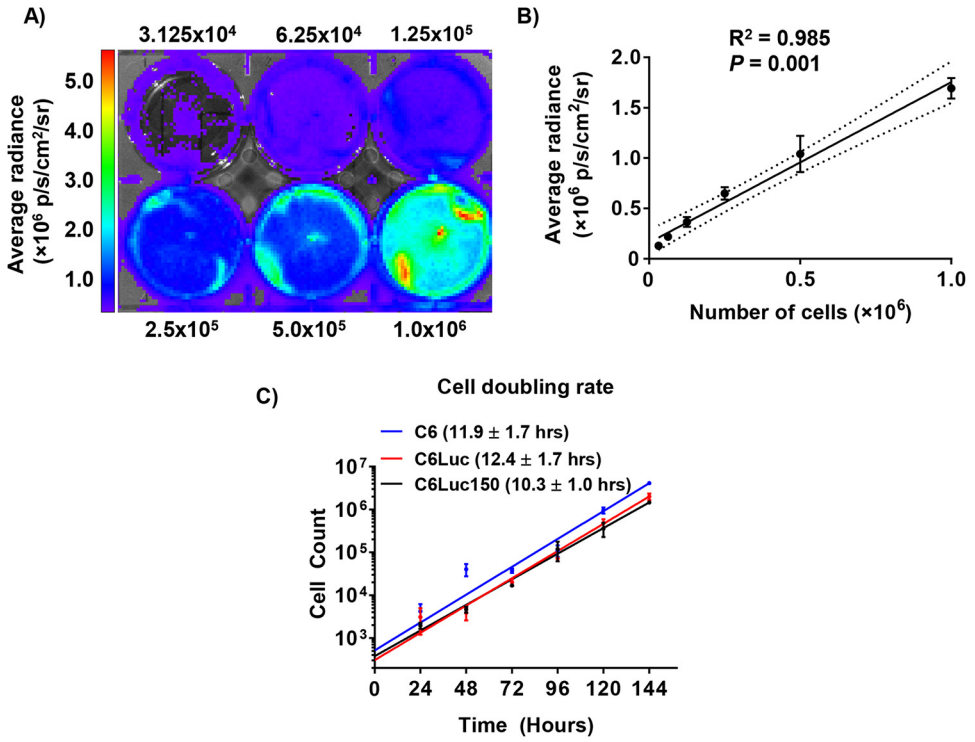

Figure 2. In vitro analysis of luciferase expression versus cell numbers, doubling rate, and luciferase activity over passage number. A representative bioluminescence image overlaid on a bright field image of a 6-well plate (n = 3) containing varying numbers of C6Luc cells, as shown (A). Image analysis showed a strong correlation between average radiance and number of cells per well (R^2 = 0.985, P = .001) (B). Doubling rates for nontransduced C6 glioma cells (n = 6), transduced C6Luc cells (n = 6), and C6Luc cells (n = 6) incubated with 150 μg/mL of D-Luciferin. No significant differences in doubling rates were noted (C).

0.5 mm, bandwidth = 62.50 kHz, NEX = 9, flip angle = 25°. Post-CE T1-weighted images were obtained ~4 minutes after Gd-DTPA injection.

Image Analysis

For BLI, the average radiance was measured by drawing a region of interest (ROI) over the head using the software Living Image (PerkinElmer). For MRI, ADC values were calculated using Functool, a vendor-provided software analysis package for brain DTI (General Electric Healthcare). Tumor volume measurements were obtained from T2-weighted and post-CE T1-weighted images using ITK-SNAP 3.6.0, a freeware image analysis tool (www.itksnap.org). Tumor boundaries, chosen on the basis of post-CE T1-weighted images, were manually contoured in ITK-SNAP and tumor volumes were calculated. If noncontrast-enhanced (NCE) regions were present within tumors, separate ROIs were drawn to measure CE and NCE tumor volumes. Microscopic images of histological sections were coregistered to post-CE T1-weighted magnetic resonance (MR) images with a nonrigid, interactive, thin-plate spline extension by Gibson in the software 3D Slicer (Surgical Planning Laboratory, Harvard Medical School, Boston, MA) (31).

Histology

At the end point (18 days post cell injection), animals were anesthetized with isoflurane and intravenously injected with pimonidazole (60 mg/kg; HypoxyProbe™-1; Hypoxyprobe Inc., MA). After 30 minutes, animals were euthanized with an overdose of isoflurane followed by a 1-mL tail-vein injection of 1-M potassium chloride to ensure cardiac arrest. Each rat was pressure-perfused through the left ventricle with 4% paraformaldehyde in a phosphate-buffered solution. Following perfusion, the brain was excised and stored at 4°C in 4% paraformaldehyde for an additional 24 hours. Brains were placed in solutions of progressively increasing glucose concentration (10%, 20%, and 30% w/v) for 1, 1 and 24 hours, respectively, embedded in optimal cutting temperature compound and frozen with a mixture of dry ice and methanol. Further 10-μm sections were obtained on a cryostat (Leica CM1860, Wetzlar, Germany) and stained for the following: hematoxylin and eosin (H&E), 4′,6-diamidino-2-phenylindole (DAPI), and hypoxia using the HypoxyProbe™-1 kit (according to manufacturer's instructions, Hyproxyprobe, Burlington, MA). Bright-field and epifluorescence microscopy was performed on an upright Zeiss Axio Imager Z1 (Carl Zeiss CG, Oberkochen, Germany).

Statistics

Statistical analyses were performed using GraphPad Prism v7 (GraphPad Software, Inc., CA). A 1-way ANOVA and Tukey post hoc test were performed to compare doubling time across conditions. For most imaging measurements over time, a 1-way repeated-measures ANOVA and Tukey post hoc test was performed. A 2-way repeated-measures ANOVA and Sidak post hoc test were performed to compare the ADC values between the CE and NCE tumor regions. For correlational analysis, Pearson product–moment analysis was performed.

RESULTS

C6Luc cells coexpressing GFP and luciferase were obtained after lentiviral transduction and 2 rounds of FACS for GFP-positive cells (Figure 1). The first FACS enabled the selection and isolation of the highest GFP-expressing cells (4.52% of all cells). In a subsequent second sort, after the first population had been expanded, cells with the top 10% fluorescence intensity were selected

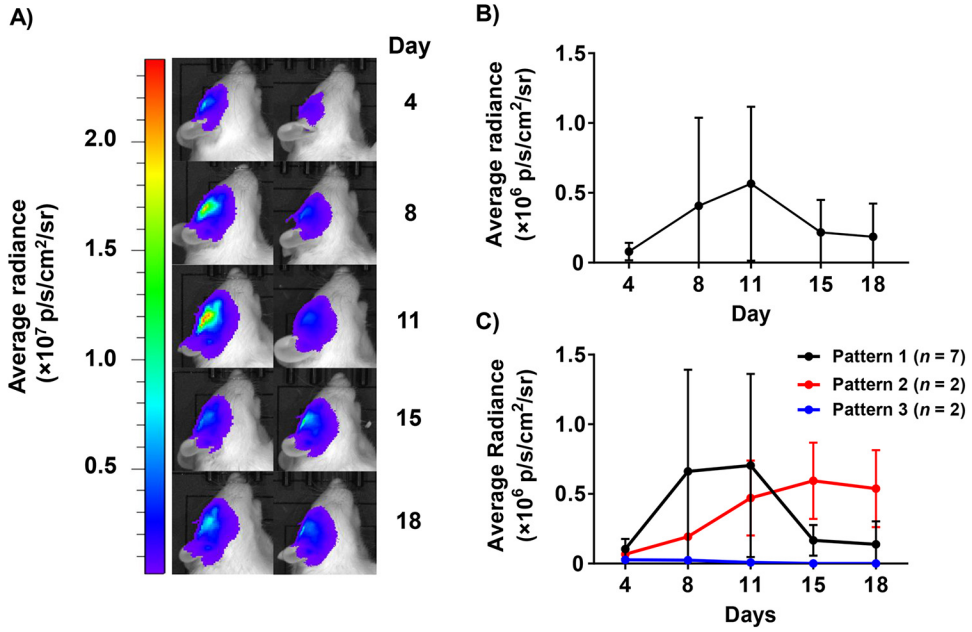

Figure 3. Bioluminescence imaging (BLI) of C6Luc orthotopic tumor growth in Wistar rats. Bioluminescence images collected from day 4 to day 18 post cell implantation. BLI images are overlaid on bright-field images of a rat lying on its left side (tumor implanted in the right side of brain) (A). Left: representative images of a rat, in which the BLI signal increased from day 4 to day 11 followed by a drop in BLI signal on days 15 and 18. Right: representative images of a rat, in which the BLI signal steadily increased and plateaued. Owing to large intersubject variability, analysis of the brain BLI signal (average radiance) revealed no significant changes with respect to time ($P > .05$) (B). The 3 BLI patterns observed between individual animals. Data are presented as mean ± SD (C).

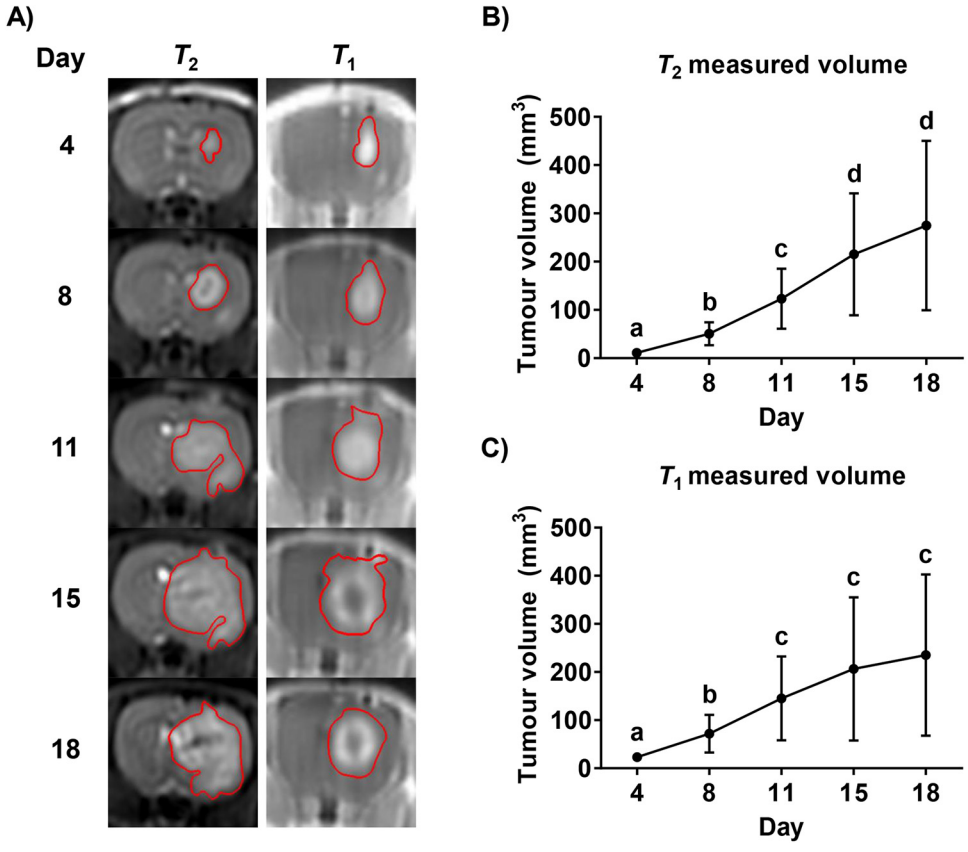

Figure 4. Representative longitudinal post-gadolinium (Gd) T1- and T2-weighted magnetic resonance imaging (MRI) of C6Luc tumor growth. T2-weighted images (left) and post-Gd T1-weighted (right) MRI of a representative animal brain showing continued tumor growth over time (A). Tumors were manually contoured (red), and total T2 (B) and T1 (C) tumor volume over time was determined ($n = 11$ rats). The letters, a, b, c, and d, denote significant differences across time points ($P < .05$). Data are presented as mean ± SD.

and expanded (Figure 1, B and D). Next, the relationship between BLI signal intensity and cell number (Figure 2, A and B), as well as the growth rates of naïve C6, C6Luc, and C6Luc150 cells (Figure 2C), was evaluated. A strong positive correlation was found between cell number and BLI signal (Figure 2, A and B; $R^2 = 0.985$, $P = .001$). No significant differences were observed between the doubling rates of C6 (11.9 ± 1.7 hours), C6Luc (12.4 ± 1.7 hours), and C6Luc150 cells (10.3 ± 1.0 h; $P = .801$).

In total, 12 Wistar rats were implanted orthotopically with 10^6 C6Luc cells and imaged with BLI and mpMRI on days 4, 8, 11, 15, and 18 following cell implantations. BLI images of a glioma-bearing rat are shown in Figure 3. Owing to significant variability across animals, no significant changes in BLI signal were detectable across time (Figure 3B; $P > .05$). However, within 7 of the 11 rats, the average radiance peaked near day 11 (group average, 5.2 ± 5.6 × 10^5 p/s/cm^2/sr) and on average dropped 2.48-fold by day 15 (group average, 2.1 ± 2.3 × 10^5 p/s/cm^2/sr) and 2.74-fold by day 18 (Figure 3C; pattern 1; group average, 1.9 ± 2.4 × 10^5 p/s/cm^2/sr). In contrast, BLI signal increased gradually and plateaued around days 15 and 18 for 2 rats (Figure 3C; pattern 2); and slowly decreased after day 4 for the other 2 rats (Figure 3C; pattern 3).

Qualitative differences in MR tumor morphology were noted across animals. Nine rats displayed tissue damage caused by the needle tract injection till the end point. Evidence of a hemorrhage was seen in 1 rat on day 11 on the basis of T2-weighted MRI, but recovery was noticed by day 18 (not shown). Tumor volumes were measured on both T2-weighted and post-CE T1-weighted MR images (Figure 4A). Total tumor volume based on T2-weighted MRI significantly increased at each time point from day 4 to day 15 (Figure 4B; $P < .05$), whereas no significant change was detected from day 15 to day 18. Post-CE T1-weighted tumor volumes exhibited a statistically significant increase from 23 ± 10 mm^3 on day 4 to 145 ± 87 mm^3 on day 11 (Figure 4C; $P < .05$), and no significant changes were detected beyond day 11. Post-CE T1- and T2-weighted tumor volumes were strongly correlated (Figure 5A; $R^2 = 0.884$, $P = .001$). When all 5 imaging time points were considered, T2-weighted tumor volume data did not correlate to BLI signal data (Figure 5B; $R^2 = 0.027$, $P = .226$) and post-CE T1-weighted tumor volume data were poorly correlated to BLI signal data (Figure 5C; $R^2 = 0.074$, $P = .045$). In contrast, T1- and T2-weighted tumor volume data from only days 4 to 11 were moderately correlated to BLI signal data (Figure 5D; $R^2 = 0.305$, $P = .001$; Figure 5E; $R^2 = 0.237$, $P = .004$), highlighting a relationship in tumor volume and BLI signal during early, but not late, tumor progression (ie, beyond day 11).

We noted in post-CE T1-weighted MR images that 7 of the 11 rodents displayed an NCE region on days 15 and 18. A repre-

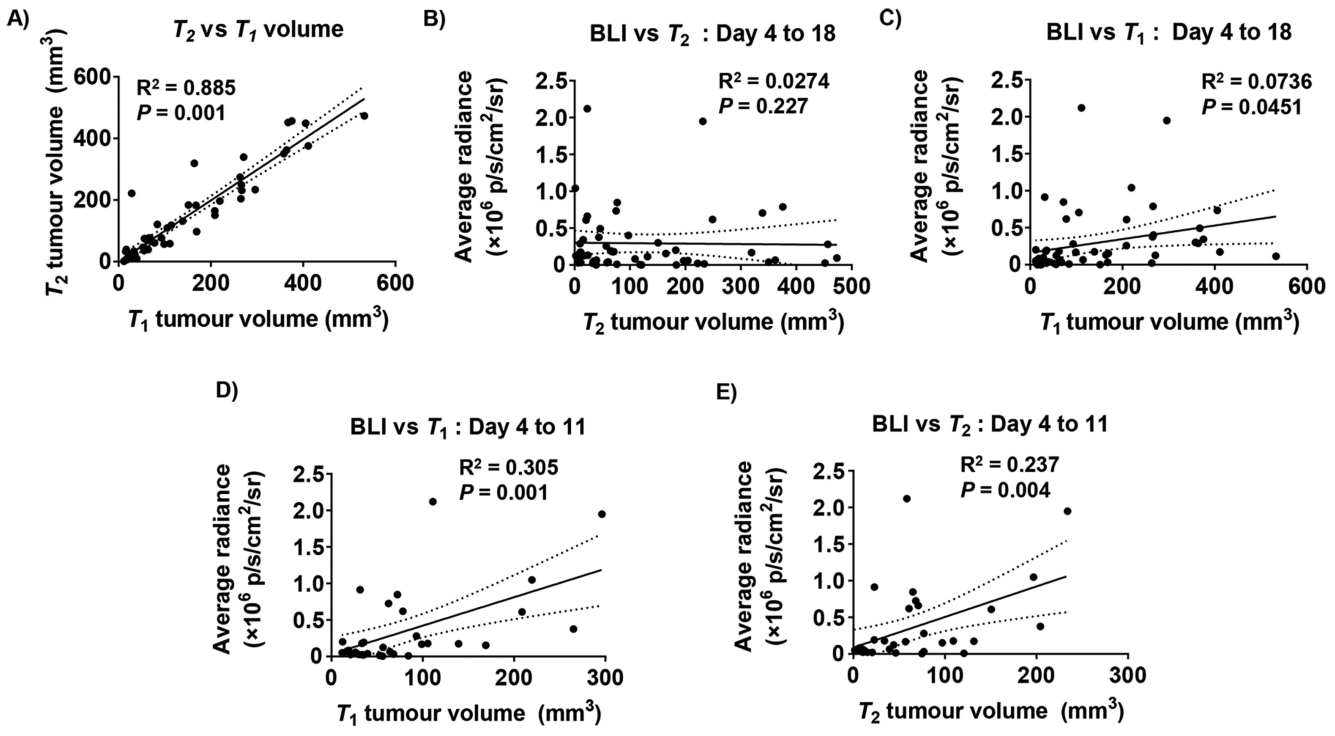

Figure 5. Correlational plots of total T2 and post-Gd T1 tumor volume to BLI signal. Post-Gd T1-weighted tumor volume was strongly correlated to T2-weighted tumor volume (A). T2 tumor volume was not correlated to BLI signal across all imaging days (4–18) (B). T1 tumor volume was poorly correlated to BLI signal across all imaging days (4–18) (C). T1 tumor volume was moderately correlated to BLI for data from days 4 to 11 only (D). T2 tumor volume was moderately correlated to BLI for data from days 4 to 11 only (E). Days 15 and 18 were excluded owing to the formation of a non-contrast-enhanced (NCE) region. The line of best fit (solid line) and the 95% confidence intervals (dotted lines) are plotted for each graph.

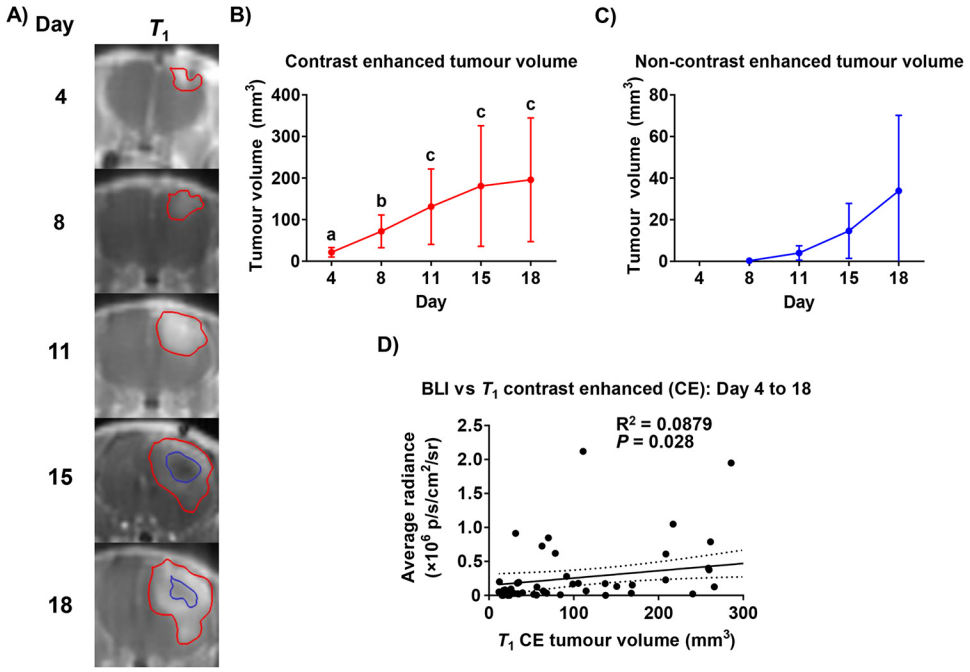

Figure 6. Longitudinal post-Gd T1-weighted MRI with contrast-enhanced (CE) and NCE regions differentiated and examined for correlation. Representative post-Gd T1-weighted magnetic resonance (MR) images of a representative rat with CE and NCE regions contoured in red and blue, respectively (A). CE tumor volume significantly increased over time (B), whereas NCE tumor volume (C) did not significantly change from days 15 and 18. T1 CE tumor volume was slightly more correlated to BLI signal when compared with T1 tumor volume, but it still had a very poor correlation (D). The line of best fit (solid line) and the 95% confidence intervals (dotted lines) are plotted. Significantly different groups are denoted by the letters, a, b, and c. All data are shown as mean ± SD.

sentative rodent is shown in Figure 6A. Therefore, we separately measured the CE and NCE tumor volumes over time. CE tumor volume significantly increased from 23 ± 10 mm^3 on day 4 to 143 ± 85 mm^3 on day 11 (Figure 6B; $P < .05$), and no significant changes were observed beyond day 11. NCE tumor volume was not significantly different between days 15 and 18 (Figure 6C). CE tumor volume data were poorly correlated to BLI signal data (Figure 7A; $R^2 = 0.088$, $P = .028$).

Next, we evaluated changes in tumor cellularity using longitudinal DTI data (Figure 7). An ADC map and matched post-CE T1-weighted MR images, with CE and NCE regions contoured, are shown in Figure 7A. On day 4, a large variability was noted in ADC values, presumably owing to tissue damage from the needle tract during the stereotactic surgery. Whole-tumor ADC values significantly increased from days 8 and 11 to day 18 (Figure 7B; $P < .05$). Of the 7 rodents that displayed NCE regions within tumors at days 15 and 18, the ADC values within these NCE regions were significantly higher than those in the surrounding CE regions (Figure 7C; $P = .001$).

MR-matched whole-brain H&E images showed large necrotic areas within tumors (Figure 8). DAPI and GFP images also showed the presence of an acellular core and many GFP-positive cells at the periphery of tumors, respectively. Pimonidazole staining showed fewer hypoxic regions, predominately adjacent to regions lacking nuclei. Coregistered ADC maps showed regions of increased ADC values that corresponded to NCE regions on post-Gd T1-weighted MR images and to necrotic regions lacking GFP-positive cells on histology.

DISCUSSION

Several groups have previously described the use of MRI-derived measures of tumor volume in the C6 model (32), and BLI has been used in some C6 tumors (33, 34). Our study describes the first combined use of mpMRI and BLI to quantitatively characterize orthotopic C6 tumor growth in rats. These 2 imaging modalities allowed longitudinal multiparametric assessment of tumor growth, including: total tumor volume; CE and NCE tumor volumes; ADC measures for whole tumor and CE and NCE regions; and relative cellular viability using BLI. Our results showed that MR measurements of tumor volume did not correlate with BLI signal beyond day 11 (Figure 5). In fact, many rats displayed a decrease in BLI signal while tumor volume continued to increase or remained stable. Previous studies have reported a linear relationship between tumor volume and BLI signal for glioma models, whereas other studies have shown a lack of a relationship (35-39). In particular, Jost et al. reported a small subset of animals ($n = 2$) showing decreased BLI signal despite increasing tumor volume and contributed it to hemorrhage and necrosis (39). Likewise, Rehemtulla et al. supported these findings and concluded that BLI signal was not always concordant with MRI tumor volume measurements, particularly for treated tumors or large untreated tumors that displayed sizeable necrotic cores (40).

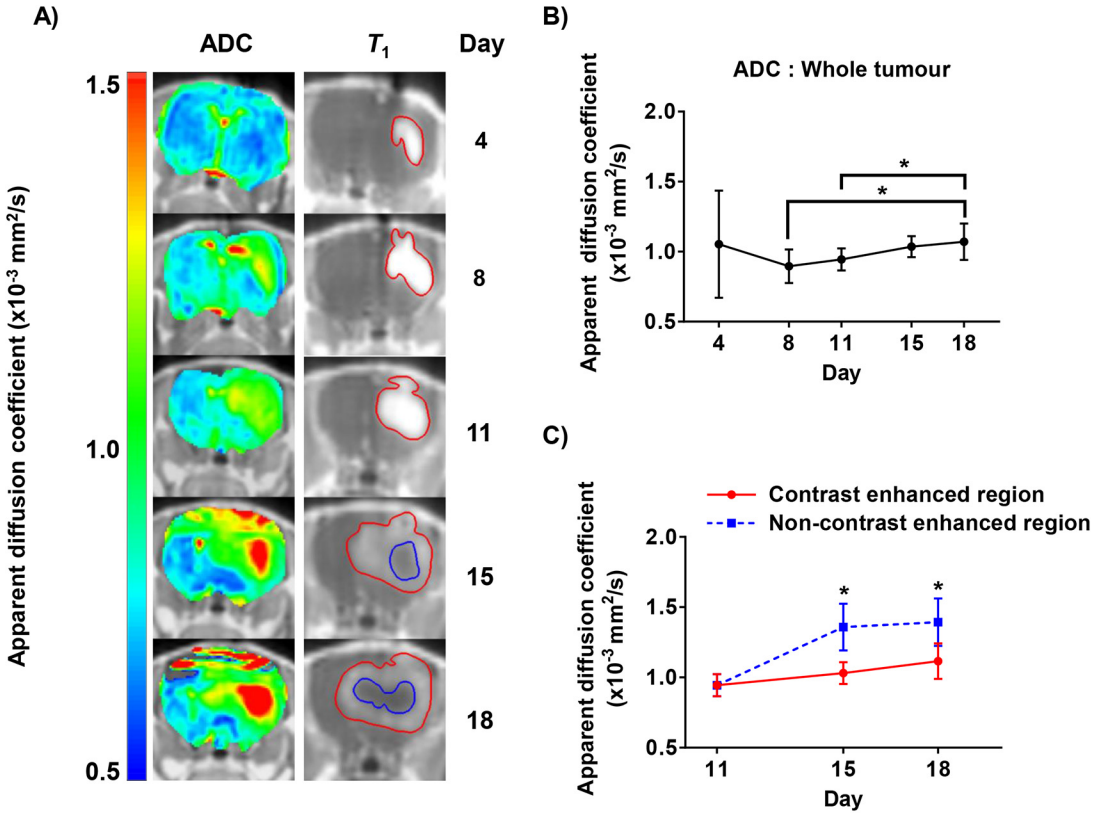

Figure 7. Longitudinal apparent diffusion coefficient (ADC) maps and post-Gd T1-weighted MRI with their respective plots. ADC maps (left) overlaid on T1-weighted MR images with CE (red) and NCE (blue) ROIs contoured (right). ADC values over the whole contoured (red) tumor plotted against time. Whole-tumor ADC values significantly increased on day 18 compared with days 8 and 11 (B). ADC values within NCE or CE regions plotted with respect to time. ADC values within NCE regions were significantly increased on both day 15 and 18 compared with ADC values in CE regions (C). The letters a and b denote significant differences at $P < .05$. All data are shown as mean ± SD.

Supported by our post-Gd T1-weighted images, ADC data, and histology, we found that beyond day 11, the day when BLI signal decreased, numerous animals formed an ill-perfused, necrotic core. Khalil et al. reported that hypoxic regions within the tumor may also have a negative influence on BLI signal, as oxygen is an important cofactor in the luciferin–luciferase reaction (41). We also found small regions of hypoxia, which were predominately adjacent to necrotic regions (Figure 8; #1 and #2). We also note that BLI only measures the viability of luciferase-expressing cancer cells, whereas tumors are composed of different types of stromal cells that can all contribute to tumor volume. There is a possibility that stromal cells growing faster than tumor cells can contribute to a larger fraction of tumor volume over time, making tumors appear larger in MR images while the BLI signal goes down. Loss of reporter expression in some of the transplanted cancer cells may also explain our results in part; however, this is less likely, as the mammalian Ubiquitin promoter used to drive reporter expression is unlikely to be silenced compared with viral promoters (eg, cytomegalovirus promoter). Realistically, it is likely that all these factors (necrosis, hypoxia, and limited substrate delivery) are contributors to the decreased BLI signal we see in our study at later time points in the majority of animals. However, combining post-Gd T1-weighted MRI, ADC mapping and BLI provides significant added value to studies that solely rely on MRI measures of tumor burden, as tumors can clearly increase in size but decrease in cellularity and overall cellular viability. Overall, our results highlight the variability in tumor growth across C6 tumor-bearing animals, as well as the value of a multimodality imaging approach to noninvasively characterize tumor development in individual animals.

Importantly, as seen in other cancer models (39, 40), changes in BLI measures of cellular viability may or may not differ from MRI measures of total tumor burden measures, meaning BLI provides complementary information to MRI for tracking tumor progression. Independently, BLI has been previously applied to the C6 model. Xi et al. used BLI to track treatment response to vincristine administered to Fischer 344 rats carrying luciferase-expressing C6 tumors in the brainstem (33, 34). Hwang et al. also applied BLI to monitor tumor growth in mice bearing luciferase-expressing C6 cells in the hind limb (42). However, our study highlights the large variability of disease progression across animals in this

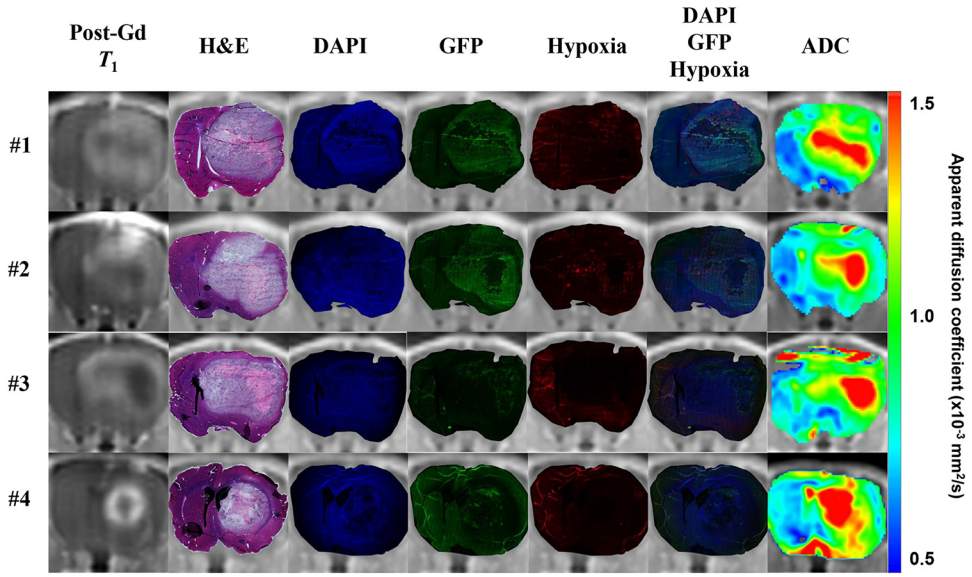

Figure 8. Fully coregistered whole-brain histology, which includes hematoxylin and eosin (H&E), 4′,6-diamidino-2-phenylindole (DAPI), GFP, and hypoxia, to post-Gd T1-weighted MR images with the respective coregistered ADC maps of 4 representative animals. Post-Gd T1-weighted MRI shows NCE and CE regions, and was the reference image for nonrigid transformation. Hematoxylin stains for positively charged structures (ie, nuclei). Eosin stains for negatively charged structures that can be found within the cell (ie, compounds and proteins commonly found in the cytoplasm). DAPI is a fluorescent dye that binds to A-T–rich regions in DNA (ie, nuclei). GFP is coexpressed with Luc, therefore only active, live cells can transcribe the gene and express the protein. Hypoxyprobe™ (pimonidazole) stains for hypoxic regions, in which the pimonidazole binds to thiol-containing proteins in hypoxic cells. DAPI, GFP, and hypoxia images were overlaid. Respective ADC maps of each animal showed an increase in ADC values within NCE regions.

model. This is important information and it highlights that studies assessing treatments can benefit from the use of combined BLI and mpMRI and analysis of response for individual animal. Similar to Response Evaluation Criteria In Solid Tumors (RECIST) criteria in humans, the evaluation of treatment response in preclinical models based solely on morphological changes in tumor volume is problematic, as volume changes can be slow to occur and this method provides little to no information on the viability of cancer cells.

A limitation of this study is the lack of histological samples obtained at each time point from different animal cohorts. Evaluation of the histological tissue could help confirm the development of hypoxia or necrosis or lack of perfusion at each time point and explain the discrepancies obtained using BLI and mpMRI over time. Furthermore, the use of additional molecular imaging tools to identify and measure tumor growth characteristics would provide a deeper understanding of tumor development in this rat model. Some examples are ^{18}F-fluorodeoxygluocose, which enables metabolic imaging of the tumor through glucose activity; ^{18}F-fluoromisonodazole, which probes regional hypoxia; and ^{18}F-galacto-arginine-glycine-aspartic acid, which is a probe for angiogenesis (43). Another imaging modality that would be useful in improving the ability to characterize tumor progression and treatment response is hyperpolarized (HP) ^{13}C magnetic resonance spectroscopic imaging (MRSI). HP ^{13}C-pyruvate MRSI is a metabolic imaging modality that measures the conversation of pyruvate to lactate, which provides information on cellular glycolysis (44). The imaging of metabolism with ^{18}F-fluorodeoxygluocose positron emission tomography or HP ^{13}C-pyruvate MRSI provides a method to monitor the biological activity of the tumor, which can be a useful surrogate measure of treatment response (45, 46).

Among the currently available intracranial glioma tumor models, there is no single model that can fully recapitulate all the distinctive characteristics of human GBM (13). The C6 glioma model has value and relevancy within this landscape because this model displays several characteristics of human GBM, such as the aggressive and diffuse infiltrative growth pattern (47), which is important for assessing therapies. In particular, Gieryng et al. concluded that the rat C6 glioma model is useful for evaluating immunotherapies that require an immunocompetent host (48). The use of our imaging tools in combination with the C6 model may be useful for evaluating current and emerging immunotherapies.

In conclusion, this was the first longitudinal study that applied mpMRI and BLI for characterizing orthotopic C6 tumor growth in rats. Future studies should apply this multimodality imaging approach to obtain as many independent, accurate, and complementary measures of tumor response to novel therapeutics.

ACKNOWLEDGMENTS

We would like to acknowledge the Biotron at Western University for their technical support and facilities. We would also like to thank Nivin Nyström for her aid supporting the animal experiments and performing BLI. This study was possible thanks to funding from the Ontario Institute for Cancer Research (TJS), Discovery Grants from the Natural Sciences and Engineering Research Council of Canada (TJS and JAR), and Startup Funding from The University of Western Ontario and the Lawson Health Research Institute (JAR).

Disclosures: No disclosures to report.

Conflict of Interest: The authors have no conflict of interest to declare.

REFERENCES

1. Canadian Cancer Society's Advisory Committee on Cancer Statistics. *Canadian Cancer Statistics 2017*. Toronto, ON: Canadian Cancer Society; 2017. Available at: cancer.ca/Canadian-Cancer-Statistics-2017-EN.pdf (accessed 05/2017).
2. Ostrom QT, Gittleman H, de Blank PM, Finlay JL, Gurney JG, McKean-Cowdin R, Stearns DS, Wolff JE, Liu M, Wolinsky Y, Kruchko C, Barnholtz-Sloan JS. American Brain Tumor Association adolescent and young adult primary brain and central nervous system tumors diagnosed in the United States in 2008-2012. Neuro Oncol. 2016;18 *Suppl. 1*:i1–i50.
3. Parsons DW, Jones S, Zhang X, Lin JC, Leary RJ, Angenendt P, Mankoo P, Carter H, Siu IM, Gallia GL, Olivi A, McLendon R, Rasheed BA, Keir S, Nikolskaya T, Nikolsky Y, Busam DA, Tekleab H, Diaz LA Jr, Hartigan J, Smith DR, Strausberg RL, Marie SK, Shinjo SM, Yan H, Riggins GJ, Bigner DD, Karchin R, Papadopoulos N, Parmigiani G, Vogelstein B, Velculescu VE, Kinzler KW. An integrated genomic analysis of human glioblastoma multiforme. Science. 2008;321:1807–1812.
4. Luwor RB, Stylli SS, Kaye AH. Using bioluminescence imaging in glioma research. J Clin Neurosci. 2015;22:779–784.
5. Nitta TSK. Prognostic implications of the extent of surgical resection in patients with intracranial malignant gliomas. Cancer. 1995;75:2727–2731.
6. Laperriere N, Zuraw L, Cairncross G; Cancer Care Ontario Practice Guidelines Initiative Neuro-Oncology Disease Site Group. Radiotherapy for newly diagnosed malignant glioma in adults: a systematic review. Radiother Oncol. 2002;64:259–273.
7. Walker MD, Green SB, Byar DP, Alexander EJ, Batzdorf U, Brooks WH, Hunt WE, MacCarty CS, Mahaley MS Jr, Mealey J Jr, Owens G, Ransohoff J 2nd, Robertson JT, Shapiro WR, Smith KR Jr, Wilson CB, Strike TA. Randomized comparisons of radiotherapy and nitrosoureas for the treatment of malignant glioma after surgery. N Engl J Med. 1980;303:1323–1329.
8. Chicoine MR, Silbergeld DL. Invading C6 glioma cells maintaining tumorigenicity. J Neurosurg. 1995;83:665–671.
9. Giese A, Bjerkvig R, Berens ME, Westphal M. Cost of migration: invasion of malignant gliomas and implications for treatment. J Clin Oncol. 2003;21:1624–1636.
10. Hanahan D, Weinberg RA. The hallmarks of cancer. Cell. 2000;100:57–70.
11. Plate KH, Risau W. Angiogenesis in malignant gliomas. Glia. 1995;15:339–347.
12. Kao HW, Chiang SW, Chung HW, Tsai FY, Chen CY. Advanced MR imaging of gliomas: an update. Biomed Res Int. 2013;2013:970586.
13. Barth RF, Kaur B. Rat brain tumor models in experimental neuro-oncology: the C6, 9L, T9, RG2, F98, BT4C, RT-2 and CNS-1 gliomas. J Neurooncol. 2009;94:299–312.
14. Jacobs VL, Valdes PA, Hickey WF, De Leo JA. Current review of in vivo GBM rodent models: emphasis on the CNS-1 tumour model. ASN Neuro. 2011;3:e00063.
15. Doblas S, Saunders D, Kshirsagar P, Pye Q, Oblander J, Gordon B, Kosanke S, Floyd RA, Towner RA. Phenyl-tert-butylnitrone induces tumor regression and decreases angiogenesis in a C6 rat glioma model. Free Radic Biol Med. 2008;44:63–72.
16. Sheehan J, Ionescu A, Pouratian N, Hamilton DK, Schlesinger D, Oskouian RJ, Jr., Sansur C. Use of trans sodium crocetinate for sensitizing glioblastoma multiforme to radiation: laboratory investigation. J Neurosurg. 2008;108:972–978.
17. Tanriover N, Ulu MO, Sanus GZ, Bilir A, Canbeyli R, Oz B, Akar Z, Kuday C. The effects of systemic and intratumoral interleukin-12 treatment in C6 rat glioma model. Neurol Res. 2008;30:511–517.
18. Benda P, Lightbody J, Sato G, Levine L, Sweet W. Differentiated rat glial cell strain in tissue culture. Science. 1968;161(3839):370–371.
19. Schmidek HH, Nielsen SL, Schiller AL, Messer J. Morphological studies of rat brain tumors induced by N-nitrosomethylurea. J Neurosurg. 1971;34:335–340.
20. Stokes AM, Hart CP, Quarles CC. Hypoxia imaging with PET correlates with antitumor activity of the hypoxia-activated prodrug evofosfamide (TH-302) in rodent glioma models. Tomography. 2016;2:229–237.
21. Qi Q, Yeung TP, Lee TY, Bauman G, Crukley C, Morrison L, Hoffman L, Yartsev S. Evaluation of CT perfusion biomarkers of tumor hypoxia. PLoS One. 2016;11:e0153569.
22. Yao NW, Chang C, Lin HT, Yen CT, Chen JY. Functional assessment of glioma pathogenesis by in vivo multi-parametric magnetic resonance imaging and in vitro analyses. Sci Rep. 2016;6:26050.
23. Weller M, Cloughesy T, Perry JR, Wick W. Standards of care for treatment of recurrent glioblastoma–are we there yet? Neuro Oncol. 2013;15:4–27.
24. Mabray MC, Barajas RF, Jr., Cha S. Modern brain tumor imaging. Brain Tumor Res Treat. 2015;3:8–23.
25. Pérez-Carro R1, Cauli O, López-Larrubia P. Multiparametric magnetic resonance in the assessment of the gender differences in a high-grade glioma rat model. EJNMMI Res. 2014;4:44.
26. Garteiser P, Doblas S, Watanabe Y, Saunders D, Hoyle J, Lerner M, He T, Floyd RA, Towner RA. Multiparametric assessment of the anti-glioma properties of OKN007 by magnetic resonance imaging. J Magn Reson Imaging. 2010;31:796–806.
27. Boult JK, Walker-Samuel S, Jamin Y, Leiper JM, Whitley GS, Robinson SP. Active site mutant dimethylarginine dimethylaminohydrolase 1 expression confers an intermediate tumour phenotype in C6 gliomas. J Pathol. 2011;225:344–352.
28. Liao J, Xia R, Liu T, Feng H, Ai H, Song B, Gao F. In vivo dynamic monitoring of the biological behavior of labeled C6 glioma by MRI. Mol Med Rep. 2013;7:1397–1402.
29. Contag CH, Ross BD. It's not just about anatomy: in vivo bioluminescence imaging as an eyepiece into biology. J Magn Reson Imaging. 2002;16:378–387.
30. Foster-Gareau P, Heyn C, Alejski A, Rutt BK. Imaging single mammalian cells with a 1.5 T clinical MRI scanner. Magn Reson Med. 2003;49:968–971.
31. Gibson, Eli, 3D fusion of histology to multi-parametric MRI for prostate cancer imaging evaluation and lesion-targeted treatment planning (2014). *Electronic Thesis and Dissertation Repository*. 2256. https://ir.lib.uwo.ca/etd/2256.
32. da Silva AC, Cabral FR, Mamani JB, Malheiros JM, Polli RS, Tannus A, Vidoto E, Martins MJ, Sibov TT, Pavon LF, Miyaki LA, Cárdenas WH, Malheiros SM, Brandt RA, Amaro Júnior E, Gamarra LF. Tumor growth analysis by magnetic resonance imaging of the C6 glioblastoma model with prospects for the assessment of magnetohyperthermia therapy. Einstein (Sao Paulo). 2012;10:11–15.
33. Xi G, Mania-Farnell B, Rajaram V, Mayanil CS, Soares MB, Tomita T, Goldman S. Efficacy of interstitial continuous vincristine infusion in a bioluminescent rodent intracranial tumor model. J Neurooncol. 2012;106:261–270.
34. Xi G, Rajaram V, Mania-Farnell B, Mayanil CS, Soares MB, Tomita T, Goldman S. Efficacy of vincristine administered via convection-enhanced delivery in a rodent brainstem tumor model documented by bioluminescence imaging. Childs Nerv Syst. 2012;28:565–574.
35. Parkins KM, Hamilton AM, Makela AV, Chen Y, Foster PJ, Ronald JA. A multimodality imaging model to track viable breast cancer cells from single arrest to metastasis in the mouse brain. Sci Rep. 2016;6:35889.
36. Baumann BC, Dorsey JF, Benci JL, Joh DY, Kao GD. Stereotactic intracranial implantation and in vivo bioluminescent imaging of tumor xenografts in a mouse model system of glioblastoma multiforme. J Vis Exp. 2012;(67). pii: 4089.
37. Ramasawmy R, Johnson SP, Roberts TA, Stuckey DJ, David AL, Pedley RB, Lythgoe MF, Siow B, Walker-Samuel S. Monitoring the growth of an orthotopic tumour xenograft model: multi-modal imaging assessment with benchtop MRI (1T), high-field MRI (9.4T), ultrasound and bioluminescence. PLoS One. 2016;11:e0156162.
38. Genevois C, Loiseau H, Couillaud F. In vivo follow-up of brain tumor growth via bioluminescence imaging and fluorescence tomography. Int J Mol Sci. 2016;17. pii: E1815.
39. Jost SC, Collins L, Travers S, Piwnica-Worms D, Garbow JR. Measuring brain tumor growth: combined bioluminescence imaging-magnetic resonance imaging strategy. Mol Imaging. 2009;8:245–253.
40. Rehemtulla A, Stegman LD, Cardozo SJ, Gupta S, Hall DE, Contag CH, Ross BD. Rapid and quantitative assessment of cancer treatment response using in vivo bioluminescence imaging. Neoplasia. 2000;2:491–495.
41. Khalil AA, Jameson MJ, Broaddus WC, Lin PS, Dever SM, Golding SE, Rosenberg E, Valerie K, Chung TD. The influence of hypoxia and pH on biolumines-

cence imaging of luciferase-transfected tumor cells and xenografts. Int J Mol Imaging. 2013;2013:287697.
42. Hwang DW, Ko HY, Lee JH, Kang H, Ryu SH, Song IC, Lee DS, Kim S. A nucleolin-targeted multimodal nanoparticle imaging probe for tracking cancer cells using an aptamer. J Nucl Med. 2010;51:98–105.
43. Kim MM, Parolia A, Dunphy MP, Venneti S. Non-invasive metabolic imaging of brain tumours in the era of precision medicine. Nat Rev Clin Oncol. 2016;13:725–739.
44. Kohler SJ, Yen Y, Wolber J, Chen AP, Albers MJ, Bok R, Zhang V, Tropp J, Nelson S, Vigneron DB, Kurhanewicz J, Hurd RE. In vivo 13 carbon metabolic imaging at 3T with hyperpolarized 13C-1-pyruvate. Magn Reson Med. 2007;58:65–69.
45. Chaumeil MM, Ozawa T, Park I, Scott K, James CD, Nelson SJ, Ronen SM. Hyperpolarized 13C MR spectroscopic imaging can be used to monitor Everolimus treatment in vivo in an orthotopic rodent model of glioblastoma. Neuroimage. 2012;59:193–201.
46. Zhu A, Lee D, Shim H. Metabolic positron emission tomography imaging in cancer detection and therapy response. Semin Oncol. 2011;38:55–69.
47. Grobben B, De Deyn PP, Slegers H. Rat C6 glioma as experimental model system for the study of glioblastoma growth and invasion. Cell Tissue Res. 2002;310:257–270.
48. Gieryng A, Pszczolkowska D, Bocian K, Dabrowski M, Rajan WD, Kloss M, Mieczkowski J, Kaminska B. Immune microenvironment of experimental rat C6 gliomas resembles human glioblastomas. Sci Rep. 2017;7:17556.